第 44 卷 第 4 期/2024 年 2 月/光学学报 研究论文

光学学报

金属光栅表面等离激元与二硫化钨激子的强耦合特性

苏盈文[1]，陆华[1*]，石首浩[1]，李顿琨[1]，王向贤[2]，赵建林[1**]

[1]西北工业大学物理科学与技术学院光场调控与信息感知工业和信息化部重点实验室，陕西省光信息技术重点实验室，陕西 西安 710129；

[2]兰州理工大学理学院，甘肃 兰州 730050

摘要 本文研究了金属光栅表面等离激元与单层二硫化钨激子的耦合共振特性。利用时域有限差分法模拟了一维金光栅/单层二硫化钨混合结构的光谱响应及电场强度分布。结果表明，金光栅表面等离激元与单层二硫化钨激子耦合可产生光谱劈裂。当改变金光栅的结构参数时，混合结构的反射光谱出现了明显的反交叉现象。采用时域耦合模理论拟合了混合结构不同参数时的反射光谱，拟合结果与数值模拟符合较好。金光栅表面等离激元与单层二硫化钨激子的耦合作用满足强耦合判据。耦合振荡器模型分析结果表明，当金光栅周期为400 nm、宽度为300 nm时，混合结构强耦合光谱的拉比劈裂为54.6 meV，其与时域耦合模理论结果一致。该工作将为表面等离激元与激子强耦合作用的深入研究与器件开发开辟新途径。

关键词 表面等离激元；一维金光栅；二硫化钨；激子；强耦合

中图分类号 O436 **文献标志码** A **DOI**：10.3788/AOS231589

1 引 言

自从单原子层材料-石墨烯成功制备以来，二维原子晶体材料（二维材料）的研究引起了人们的广泛关注[1-10]。二维材料具有优异的光电、机械及化学性能，在电子、光电子及光子学等领域展现出重要的应用前景[11-17]。如今，已发现的二维材料约60种，包括石墨烯、六方氮化硼、黑磷及过渡金属硫化物等[18-19]。二维材料具有量子限域效应，可使其激子结合能显著增加。作为重要的二维材料，过渡金属硫化物拥有独特的性质，例如单层过渡金属硫化物为直接带隙半导体，其激子拥有谷自由度，具有较大的跃迁偶极矩和结合能，并且易调控、稳定性强[20-21]。过渡金属硫化物二维材料将为共振腔光子与激子强耦合效应及其器件开发起到重要的推动作用[22]。传统光学腔共振线宽小、品质因子高，但难以将模式体积减小到光学衍射极限以下。金属纳米结构表面等离激元可突破衍射极限，光场局域在亚波长范围内，拥有较小的模式体积，成为实现光子与激子强耦合作用的重要手段[22-24]。光子与激子发生强耦合时，会形成半光、半物质的极化激元态[22]，在室温玻色-爱因斯坦凝聚[25-26]、量子信息处理[27]、非线性效应[28]等领域具有重要的应用价值。金属纳米结构表面等离激元与过渡金属硫化物激子的结合，为实现纳米尺度极化激元态及其应用开辟了新途径。

近年来，国内外研究者在金属表面等离激元与过渡金属硫化物激子强耦合作用方面开展了一些研究工作，取得了一定的研究进展。首先，金属纳米阵列与过渡金属硫化物的结合为表面等离激元-激子强耦合的产生提供了可能。例如：王绍军等[29]将金属纳米孔阵列与单层二硫化钨结合，在室温下观测到表面等离激元与单层二硫化钨激子的强耦合作用及60 meV的拉比劈裂；随后，方哲宇等[30]将银纳米盘阵列/单层二硫化钨异质结构嵌入光学共振腔，产生了光子与激子极化激元混合态，得到300 meV的拉比劈裂，大幅提高了拉比劈裂能量；另外，果尚志等[31]在啁啾银纳米槽阵列/单层二硫化钨结构中观测到表面等离激元与激子的强耦合作用，并基于此实现了极化非厄米特系统。同时，单金属纳米颗粒因较小的模式体积也成为研究表面等离激元与激子强耦合的重要结构。例如：张顺平等[32]将银纳米棒与单层二硒化钨进行有机结合，在单金属纳米腔中实现了表面等离激元与激子的强耦合，获得了49.5 meV的拉比劈裂；为提高强耦合拉比

收稿日期：2023-09-21；**修回日期**：2023-11-11；**录用日期**：2023-12-13；**网络首发日期**：2023-12-23

基金项目：国家自然科学基金（11974283，11774290，61705186）、“双一流”高校建设基金（0206022GH0202）、中央高校基本科研业务费项目（D5000220175）

通信作者：*hualu@nwpu.edu.cn；**jlzhao@nwpu.edu.cn

劈裂能量，陆培祥等[33]将银纳米立方体和银膜组成的表面等离激元纳米腔与单层二硫化钨相结合，在暗场散射谱中观察到了模式的分裂现象，实现了拉比劈裂能量为 145 meV 的强耦合作用；除了单层过渡金属硫化物，Geisler 等[34]实验证实了单晶金纳米盘与多层二硫化钨结合也可产生表面等离激元-激子强耦合作用，得到了 175 meV 的拉比劈裂；许秀来等[35]在单金蝴蝶结/八层二硫化钼系统中实现了表面等离激元与激子的强耦合作用，其拉比劈裂能量为 110 meV，并在八层二硫化钼中观测到耦合激子数为 48；此外，罗宇等[36]将金蝴蝶结制备成阵列结构，在金蝴蝶结阵列与单层二硫化钨混合系统中实现了表面等离激元与激子的强耦合作用，其拉比劈裂能量达到 118 meV。上述研究工作为探明表面等离激元与激子强耦合的产生方法及机理起到重要推动作用。金属表面等离激元结构与过渡金属硫化物的结合为少激子甚至单激子强耦合提供了可能，将促进室温量子光学、非线性光学、光电调制器件等方面的发展[37-39]。金属光栅作为典型的表面等离激元结构之一，相比二维金属纳米阵列，结构更简单，被广泛用于微纳光子器件的制备。然而，金属光栅表面等离激元与过渡金属硫化物激子的耦合效应还有待进一步研究。

本文开展了基于一维金光栅与单层二硫化钨混合结构的表面等离激元与激子耦合共振特性的研究。研究发现，当改变金光栅的结构参数时，反射光谱呈现出明显的反交叉现象。金光栅表面等离激元与单层二硫化钨激子的耦合作用满足严格的强耦合判据，形成极化激元态。耦合振荡器模型分析结果表明，当金光栅周期为 400 nm、宽度为 300 nm 时，反射谱的拉比劈裂为 54.6 meV，这与时域耦合模理论结果相符。该研究工作将有助于金属光栅表面等离激元与激子耦合效应的深入探索及器件开发。

2 理论模型

图 1(a)为金属光栅与过渡金属硫化物的混合结构示意图。该混合结构由单层二硫化钨、一维金光栅及二氧化硅衬底构成。如图所示，p、l 和 h 分别表示金光栅的周期、宽度和高度。二氧化硅和金的光学常数可参见材料手册[40-41]。其中，金的介电常数也可由 Drude 模型进行描述：$\varepsilon_{\mathrm{Au}}(\omega)=\varepsilon_{\infty,m}-\omega_{\mathrm{P}}^2/\omega(\omega+\mathrm{i}\omega_{\mathrm{c}})$，其中 $\varepsilon_{\infty,m}$ 为高频相对介电常数，其值为 $\varepsilon_{\infty,m}=9.5$；$\omega_{\mathrm{p}}$ 和 ω_{c} 分别为金的等离子体振荡频率和碰撞频率，其值分别为 $\omega_{\mathrm{p}}=8.949$ eV 和 $\omega_{\mathrm{c}}=0.069$ eV[42]；ω 为入射光的角频率。单层过渡金属硫化物的介电常数可由高阶洛伦兹模型进行描述[43]，即

$$\varepsilon_{\mathrm{WS_2}}(\omega)=\varepsilon_{\infty}+\sum_{j=1}^{N}\frac{a_j}{\omega_j^2-\omega^2-\mathrm{i}\omega b_j},\tag{1}$$

式中：ε_{∞} 为直流介电常数；ω_j、a_j 及 b_j 分别代表第 j 个振荡器的共振频率、振荡功率及阻尼因子。由实验结果可知，单层二硫化钨的介电常数的相关参数 $\varepsilon_{\infty}=7.449$，$\omega_j$、$a_j$ 及 b_j 的值如表 1 所列[43]。

表 1 单层二硫化钨介电常数的相关参数

Table 1 Related parameters of dielectric constant of monolayer tungsten disulfide

j	ω_j /eV	a_j /eV^2	b_j /eV
1	2.011	1.870	0.029
2	2.404	3.550	0.186
3	2.834	8.416	0.225
4	3.131	42.800	0.639

金光栅表面等离激元与单层二硫化钨激子的耦合光谱特性可采用时域耦合模理论描述[44]。若取金光栅表面等离激元和单层二硫化钨激子共振模式的振幅分别为 a 和 b，则其演化方程[45]可写为

$$\frac{\mathrm{d}a}{\mathrm{d}t}=(-\mathrm{i}\omega_a-\gamma_{11}-\gamma_{12})a+S_{\mathrm{i}}\sqrt{\gamma_{11}}-\mathrm{i}gb,\tag{2}$$

$$\frac{\mathrm{d}b}{\mathrm{d}t}=(-\mathrm{i}\omega_b-\gamma_2)b-\mathrm{i}ga,\tag{3}$$

式中：ω_a 和 ω_b 分别为金光栅表面等离激元和单层二硫化钨激子的共振频率；γ_{11} 和 γ_{12} 分别为金光栅表面等离激元由辐射和损耗引起的衰减率，其和 $\gamma_{11}+\gamma_{12}=\gamma_1$ 为金光栅的总衰减率；γ_2 表示单层二硫化钨激子共振损耗而引起的衰减率；g 为表面等离激元与激子的耦合强度；S_{i}、S_{r} 分别为入射、反射光波能量，入射和反射光波满足关系式：$S_{\mathrm{r}}=-S_{\mathrm{i}}+a\sqrt{\gamma_{11}}$。当衰减率与共振频率满足 γ_{12}、$\gamma_2\ll\gamma_{11}\ll\omega_a$ 及 $\omega-\omega_a\ll\omega_a$ 时，混合结构的反射谱[45]可表示为

$$R=\left|\frac{S_{\mathrm{r}}}{S_{\mathrm{i}}}\right|^2=\left|\frac{\gamma_{11}}{\mathrm{i}(\omega_a-\omega)+\gamma_1+g^2/\left[\mathrm{i}(\omega_b-\omega)+\gamma_2\right]}-1\right|^2。\tag{4}$$

3 结果分析

首先利用 FDTD 软件构建时域有限差分数值模型，模拟计算了金光栅/单层二硫化钨混合结构的光谱响应及电场分布情况[46]。模型中将 x 轴方向设置为周期性边界条件，y 轴方向设置为完美匹配层边界条件[47]。入射光为偏振方向垂直于金光栅的平面光波。单层二硫化钨的厚度设为 0.618 nm[43]。初始结构参数设置为 $p=400$ nm，$l=300$ nm，$h=95$ nm。金、单层二硫化钨等材料的介电常数均为室温下测得的参数[41,43]。需要注意的是，当温度发生变化或入射光强度较大(引起强的热积累效应)时，金属材料的介电常数会发生变化，进而可能对结果产生一定影响[48-50]。

图 1(b)为有无单层二硫化钨时金光栅的反射光

谱。由图可知，金光栅结构的光谱在620 nm处出现了明显的反射谷。图1(c)显示了金光栅在620 nm波长处的电场强度分布。由图可知，电场能量主要局域在金光栅顶点，产生了局域表面等离激元共振[51]。图1(b)插图为单层二硫化钨的反射光谱，可以看出，在620 nm处出现了反射峰，其位于单层二硫化钨A激子波长处。当单层二硫化钨覆盖于金光栅时，混合结构的反射光谱将产生劈裂，在原反射谷的620 nm处出现了明显的反射峰，两侧劈裂为两个反射谷。图1(d)给出了金光栅/单层二硫化钨混合结构在620 nm处的电场强度分布情况，其中白色虚线为单层二硫化钨的位置。由图可知，电场能量局域于金光栅顶点，覆盖二硫化钨后，电场强度明显减弱。上述光谱劈裂现象源于表面等离激元与单层二硫化钨激子的相互耦合[52]。

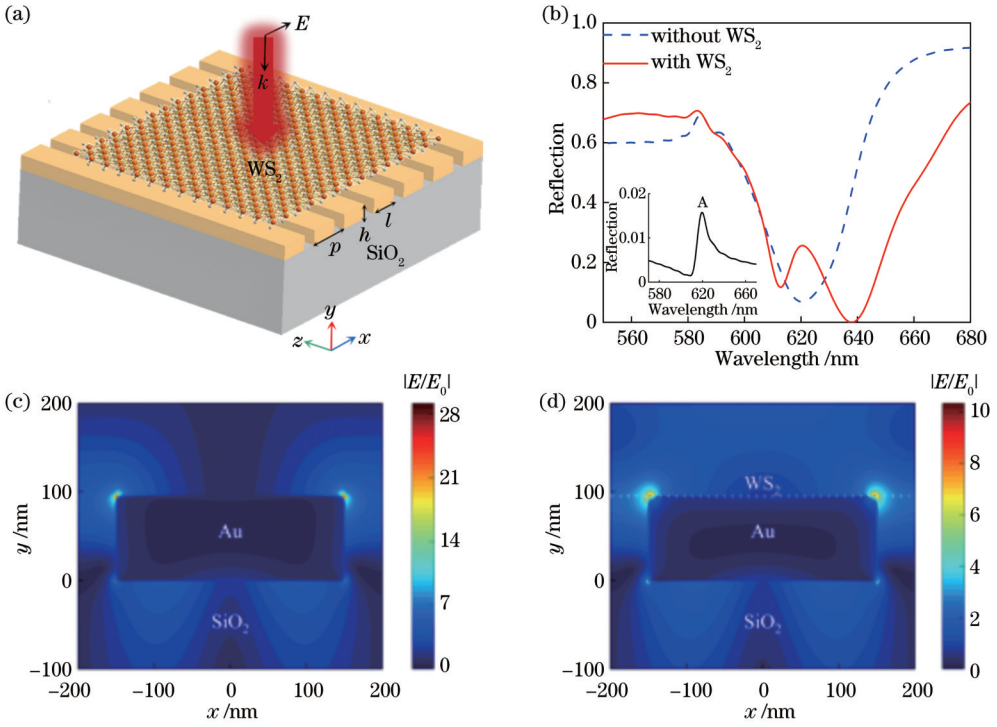

图1　一维金光栅与单层二硫化钨混合结构及其反射光谱与场分布。(a)金光栅/单层二硫化钨混合结构示意图；(b)当金光栅周期p、宽度l、高度h分别为400、300、95 nm时，金光栅结构、金光栅/单层二硫化钨混合结构的反射光谱，插图为单层二硫化钨的反射光谱；(c)金光栅结构在反射谷波长620 nm处的电场强度分布$|E/E_0|$；(d)金光栅/单层二硫化钨混合结构在反射峰波长620 nm处的电场强度分布$|E/E_0|$

Fig. 1　Hybrid structure consisting of a one-dimensional gold grating and a monolayer tungsten disulfide and its reflection spectrum and field distribution. (a) Schematic of hybrid structure with gold grating and monolayer tungsten disulfide; (b) reflection spectra of gold grating structure and gold grating/monolayer tungsten disulfide hybrid structure with grating pitch p=400 nm, width l=300 nm, and height h=95 nm. Inset shows reflection spectrum of a monolayer tungsten disulfide; (c) distribution of electric field $|E/E_0|$ in gold grating structure at reflection dip wavelength of 620 nm; (d) distribution of electric field $|E/E_0|$ of gold grating/monolayer tungsten disulfide hybrid structure at reflection peak wavelength of 620 nm

为探究金光栅结构参数对表面等离激元与单层二硫化钨激子耦合作用的影响，模拟计算了金光栅/单层二硫化钨混合结构在不同光栅周期、宽度及高度时的反射光谱，并与金光栅的反射光谱进行了对比。首先，使用时域有限差分法模拟了金光栅结构、金光栅/单层二硫化钨混合结构不同周期时的反射光谱，如图2(a)和2(b)中实线所示。当光栅宽度l=300 nm、光栅高度h=95 nm时，光栅周期p从380 nm增至400 nm，金光栅的反射谷位置由607 nm增至620 nm。相比金光栅，覆盖单层二硫化钨的金光栅结构在原反射谷处皆存在反射峰。随着金光栅周期的增加，反射光谱发生改变，但反射峰的位置几乎不发生变化，这源于激子诱导的反射峰不受金光栅结构变化的影响。混合结构反射光谱随光栅周期的变化主要源于表面等离激元共振波长的改变。通过非线性最小二乘法，结合式(4)对金光栅/单层二硫化钨混合结构的反射光谱进行拟合，如图2(b)中虚线所示，拟合光谱与模拟光谱符合较好。

模拟了金光栅结构及金光栅/单层二硫化钨混合结构的反射光谱随光栅宽度l的变化情况，结果如图3(a)和3(b)中实线所示。其中取光栅周期p=400 nm，光栅高度h=95 nm。可以看出，当光栅宽度l从290 nm增至310 nm时，金光栅反射谷随l的增加发生红移，反射谷位置从618 nm增至623 nm。同样，覆

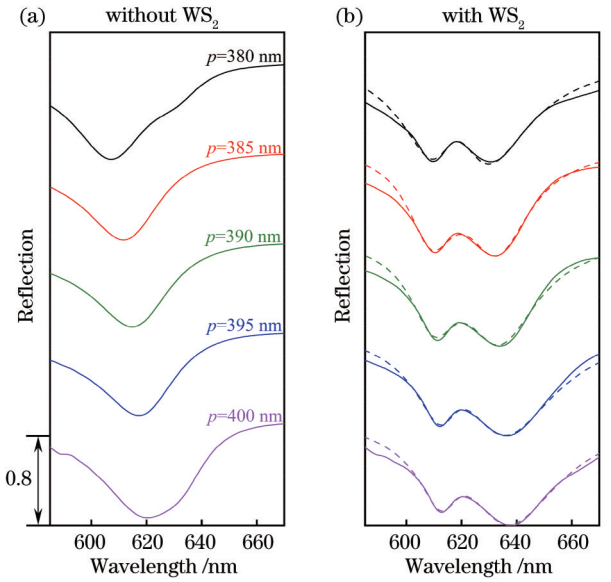

图 2　金光栅反射光谱与光栅周期的关系。(a)金光栅结构不同周期时的反射光谱;(b)含单层二硫化钨的金光栅不同周期时的反射光谱(实线)和时域耦合模理论拟合的反射光谱(虚线)。其他参数为 l=300 nm,h=95 nm

Fig. 2　Relationship between reflection spectrum of gold grating and grating pitches. (a) Reflection spectra of gold grating structures with different pitches p; (b) reflection spectra of gold grating/monolayer tungsten disulfide hybrid structures with different p (solid lines) and reflection spectra fitted by temporal coupled-mode theory (dashed lines). Other parameters are set as l=300 nm and h=95 nm

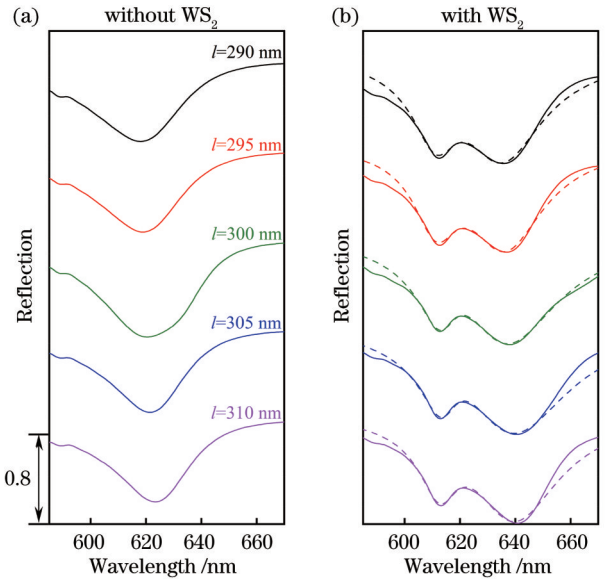

图 3　金光栅反射光谱与光栅宽度的关系。(a)金光栅结构不同宽度时的反射光谱;(b)含单层二硫化钨的金光栅不同宽度时的反射光谱(实线)和理论拟合的反射光谱(虚线)。其他参数为 p=400 nm,h=95 nm

Fig. 3　Relationship between reflection spectrum of gold grating and grating widths. (a) Reflection spectra of gold grating structures with different widths l; (b) reflection spectra of gold grating/monolayer tungsten disulfide hybrid structures with different l (solid lines) and theoretically fitted reflection spectra (dashed lines). Other parameters are set as p=400 nm and h=95 nm

盖单层二硫化钨后金光栅的反射光谱发生劈裂,产生了不随光栅宽度变化的反射峰。图 3(b)中虚线为利用式(4)对上述反射光谱进行拟合的结果,拟合光谱与模拟光谱符合较好。

随后,研究了混合结构的反射光谱随金光栅高度 h 的变化情况。图 4(a)和 4(b)显示了金光栅结构和金光栅/单层二硫化钨混合结构在金光栅高度取不同值时(从 70 nm 到 95 nm)的反射光谱。金光栅周期和宽度分别为 p=400 nm 和 l=300 nm。由图可知,金光栅的反射谷随高度 h 增加发生红移。覆盖单层二硫化钨后,金光栅的劈裂光谱随光栅高度增加呈现反交叉现象。图 4(b)中实线为数值模拟结果,虚线为时域耦合模理论拟合的结果,可见拟合光谱与模拟光谱符合较好。图 5 为时域耦合模理论拟合的参数(表面等离激元共振频率 ω_a、耦合强度 g,及衰减率 γ_1 和 γ_2)随光栅高度的变化情况。由图可知,耦合强度 g、衰减率 γ_1 和 γ_2 对金光栅高度变化不敏感,分别约为 27.3、62.8、17.8 meV。对于反射光谱劈裂与反交叉现象,可利用耦合振荡器模型对表面等离激元与激子耦合作用进行描述,其关系式[52]可写为

$$\begin{pmatrix} \omega_a - \mathrm{i}\dfrac{\gamma_1}{2} & g \\ g & \omega_b - \mathrm{i}\dfrac{\gamma_2}{2} \end{pmatrix} \begin{pmatrix} \alpha \\ \beta \end{pmatrix} = \omega \begin{pmatrix} \alpha \\ \beta \end{pmatrix}, \tag{5}$$

式中:α 和 β 为霍普菲尔德系数;其他参数与式(4)相同。由式(5)可得光谱劈裂能量特征值[52]为

$$\omega_{\pm} = \frac{\omega_a + \omega_b}{2} \pm \frac{1}{2}\sqrt{4g^2 + \left(\delta - \mathrm{i}\frac{\gamma_1 - \gamma_2}{2}\right)^2} - \mathrm{i}\frac{\gamma_1 + \gamma_2}{4}, \tag{6}$$

式中,$\delta = \omega_a - \omega_b$ 为表面等离激元和激子共振频率的失谐。劈裂能量差(即拉比劈裂能量)为

$$\Omega = \omega_+ - \omega_- = \sqrt{4g^2 + \left(\delta - \mathrm{i}\frac{\gamma_1 - \gamma_2}{2}\right)^2}。 \tag{7}$$

当拉比劈裂能量超过表面等离激元和激子衰减率的平均值$\left(\text{即}\Omega > \dfrac{\gamma_1 + \gamma_2}{2}\right)$时,表面等离激元与激子耦合作用处于强耦合区域。此时,光谱劈裂反射谷分别对应上极化激元(upper polariton, UP)分支和下极化激元(lower polariton, LP)分支。利用上述耦合振荡器模型对反射光谱劈裂能量进行拟合,发现劈裂能量与失谐 δ 呈现典型的反交叉行为,光谱劈裂能量与拟

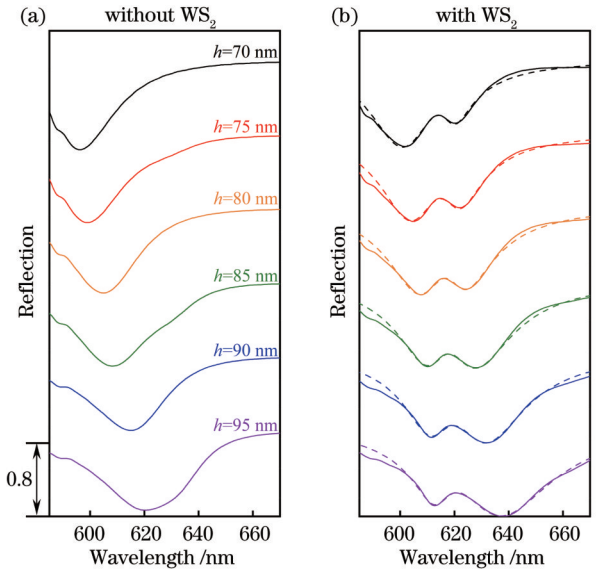

图 4　金光栅反射光谱与光栅高度的关系。(a)金光栅结构不同高度时的反射光谱;(b)含单层二硫化钨的金光栅不同高度时的反射光谱(实线)和理论拟合的反射光谱(虚线)。其他参数为 p=400 nm,l=300 nm

Fig. 4　Relationship between reflection spectrum of gold grating and grating heights. (a) Reflection spectra of gold grating structures with different heights h; (b) reflection spectra of gold grating/monolayer tungsten disulfide hybrid structures with different h (solid lines) and theoretically fitted reflection spectra (dashed lines). Other parameters are set as p=400 nm and l=300 nm

合结果符合较好,如图 6(a)所示。在失谐 δ 为零时,Ω=54.6 meV。因 γ_1 和 γ_2 分别约为 62.8 meV 和 17.8 meV,耦合作用满足强耦合条件 $\Omega>\frac{\gamma_1+\gamma_2}{2}$。因此,金光栅表面等离激元与单层二硫化钨激子的耦合属于强耦合作用,形成极化激元态,拉比劈裂能量为 54.6 meV,与时域耦合模理论结果(g=27.3 meV)相符,即 $\Omega=2g$。该结构的拉比劈裂能量与银纳米槽/单层二硫化钨等混合结构相近[31-32]。图 6(b)显示了 UP 分支中表面等离激元与激子的占比情况。可以看出,随着失谐 δ 的增加,表面等离激元的占比逐渐增大,激子的占比逐渐减小,当失谐为零时,两者占比相同。

最后,研究了环境折射率 n 的变化对金光栅/单层二硫化钨混合结构反射光谱的影响。如图 7 所示,当 p=400 nm、l=300 nm、h=105 nm 时,金光栅/单层二硫化钨混合结构反射光谱随折射率增加发生明显变化。随着折射率的增加,UP 分支对应的反射谷位置几乎不发生改变,LP 分支对应的反射谷发生明显红移。两反射谷波长差 $\Delta\lambda$ 将随折射率的增加而变大,几乎呈线性关系,如插图所示。因此,该混合结构产生的强耦合光谱劈裂将为折射率光学传感的实现提供一种新方法[53]。

4　结　　论

一维金属光栅作为重要的表面等离激元结构之一,相比二维金属纳米阵列,结构更简单,相较于单金属纳米颗粒,更适合制备较大面积的光子器件。本文研究了一维金光栅与单层二硫化钨混合结构中表面等离激元与激子的耦合特性。通过构建时域有限差分数

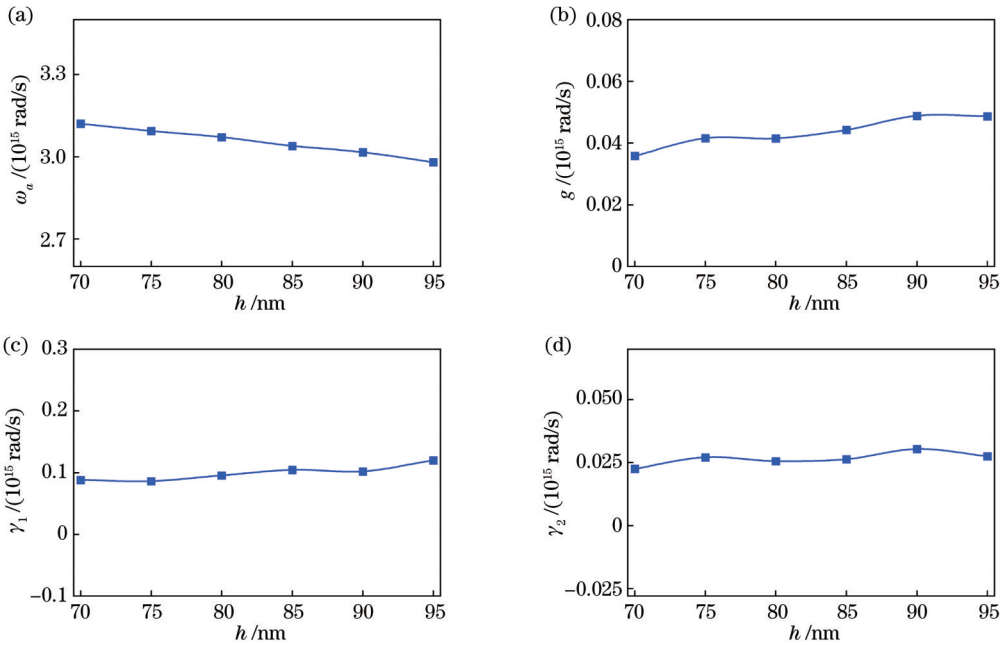

图 5　时域耦合模理论拟合参数。理论拟合的(a)表面等离激元共振频率 ω_a、(b)耦合强度 g、(c)衰减率 γ_1 及(d)衰减率 γ_2 随金光栅高度 h 的变化情况

Fig. 5　Parameters fitted by temporal coupled-mode theory. Theoretically fitted (a) plasmonic resonance frequency ω_a, (b) coupling strength g, (c) decay rate γ_1, and (d) decay rate γ_2 varying with gold grating heights h

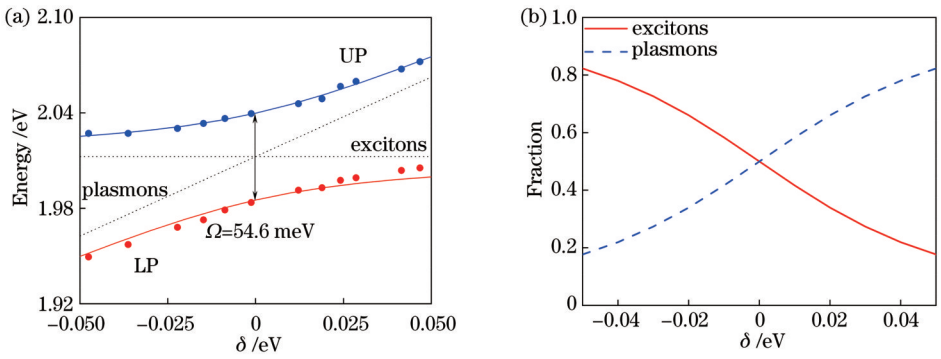

图 6 金光栅表面等离激元与单层二硫化钨激子的强耦合作用。(a)金光栅/单层二硫化钨混合结构中表面等离激元与激子耦合的光谱劈裂能量UP分支(上方的圆点)和LP分支(下方的圆点)随失谐δ的变化情况。实线为耦合振荡器模型拟合值;(b)UP分支中表面等离激元与激子占比随失谐δ的变化情况

Fig. 6 Strong coupling between surface plasmons in gold grating and excitons in monolayer tungsten disulfide. (a) Splitting energy UP (dots above) and LP (dots below) branches in coupling between surface plasmons and excitons in gold grating/monolayer tungsten disulfide hybrid structure varying with detuning δ. Solid curves denote fitting results by coupled oscillator model; (b) fractions of surface plasmons and excitons in UP branch varying with detuning δ

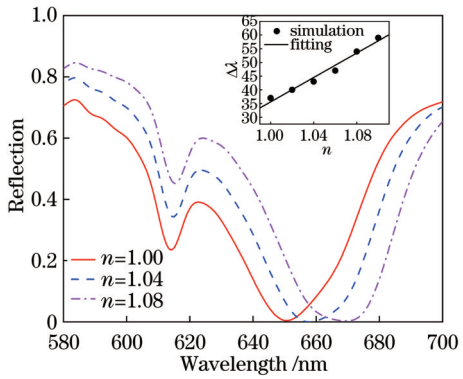

图 7 金光栅周期、宽度、高度分别为400、300、105 nm时,金光栅/单层二硫化钨混合结构在不同环境折射率条件下的反射光谱。插图为反射谷波长差$\Delta\lambda$与折射率n的关系,圆点、实线分别为模拟、拟合结果

Fig. 7 Reflection spectra of gold grating/monolayer tungsten disulfide hybrid structure with different environmental refractive indices when p, l, and h of gold grating are 400, 300, and 105 nm, respectively. Inset shows relationship between reflection dip wavelength difference $\Delta\lambda$ and refractive index n. Dots denote simulation results and solid line denotes fitting result

值模型,计算了金光栅结构、金光栅/单层二硫化钨混合结构的反射光谱及电场强度分布,探明了其随金光栅结构参数(光栅周期、宽度及高度)改变的变化规律。结果表明,单层二硫化钨的引入使金光栅表面等离激元共振反射谷出现明显劈裂,这源于表面等离激元与二硫化钨激子的耦合作用。通过改变结构参数,反射光谱劈裂能量出现反交叉现象。由时域耦合模理论及耦合振荡器模型分析可知,金光栅表面等离激元与单层二硫化钨激子耦合作用处于强耦合区域。当金光栅周期和宽度分别为400 nm和300 nm时,拉比劈裂能量为54.6 meV。金光栅/单层二硫化钨混合结构产生的极化激元态中表面等离激元与激子占比随其失谐变化而改变,例如上极化激元(UP)分支中表面等离激元、激子占比分别随失谐增加出现递增、递减现象。最后,探究了环境折射率变化对金光栅/单层二硫化钨混合结构反射光谱的影响,发现两反射谷波长差与折射率近似呈线性关系。该工作将为表面等离激元与激子强耦合的产生与器件(如光学传感器)开发提供新方案。

参 考 文 献

[1] Novoselov K S, Geim A K, Morozov S V, et al. Electric field effect in atomically thin carbon films[J]. Science, 2004, 306(5696): 666-669.

[2] Zhang Y B, Tan Y W, Stormer H L, et al. Experimental observation of the quantum Hall effect and Berry's phase in graphene[J]. Nature, 2005, 438: 201-204.

[3] Neto A H C, Guinea F, Peres N M R, et al. The electronic properties of graphene[J]. Reviews of Modern Physics, 2009, 81(1): 109-162.

[4] Huang X, Zeng Z Y, Zhang H. Metal dichalcogenide nanosheets: preparation, properties and applications[J]. Chemical Society Reviews, 2013, 42(5): 1934-1946.

[5] Chhowalla M, Liu Z F, Zhang H. Two-dimensional transition metal dichalcogenide (TMD) nanosheets[J]. Chemical Society Reviews, 2015, 44(9): 2584-2586.

[6] Lu H, Yue Z J, Li Y W, et al. Magnetic plasmon resonances in nanostructured topological insulators for strongly enhanced light - MoS_2 interactions[J]. Light: Science & Applications, 2020, 9: 191.

[7] Guo J S, Li J, Liu C Y, et al. High-performance silicon—graphene hybrid plasmonic waveguide photodetectors beyond 1.55 μm[J]. Light: Science & Applications, 2020, 9: 29.

[8] Li D K, Lu H, Li Y W, et al. Plasmon-enhanced photoluminescence from MoS_2 monolayer with topological insulator nanoparticle[J]. Nanophotonics, 2022, 11(5): 995-1001.

[9] Hou L P, Wang Q F, Zhang H M, et al. Simultaneous control of plasmon-exciton and plasmon-trion couplings in an Au nanosphere and monolayer WS_2 hybrid system[J]. APL Photonics, 2022, 7(2): 026107.

[10] Tan H, Du L, Yang F H, et al. Two-dimensional materials in

photonic integrated circuits: recent developments and future perspectives[J]. Chinese Optics Letters, 2023, 21(11): 110007.
[11] Wang Q H, Kalantar-Zadeh K, Kis A, et al. Electronics and optoelectronics of two-dimensional transition metal dichalcogenides[J]. Nature Nanotechnology, 2012, 7: 699-712.
[12] Xia F N, Wang H, Xiao D, et al. Two-dimensional material nanophotonics[J]. Nature Photonics, 2014, 8: 899-907.
[13] 柯宇轩, 岑颖乾, 綦殿禹, 等. 基于二维材料的光通信波段光电探测器[J]. 中国激光, 2023, 50(1): 0113008.
Ke Y X, Cen Y Q, Qi D Y, et al. Two-dimensional materials photodetectors for optical communications[J]. Chinese Journal of Lasers, 2023, 50(1): 0113008.
[14] 黎志文, 陆华, 李扬武, 等. 光学薄膜塔姆态诱导石墨烯近红外光吸收增强[J]. 光学学报, 2019, 39(1): 0131001.
Li Z W, Lu H, Li Y W, et al. Near-infrared light absorption enhancement in graphene induced by the Tamm state in optical thin films[J]. Acta Optica Sinica, 2019, 39(1): 0131001.
[15] 张佩茹, 刘欢, 胡加兴, 等. 单层 $MoS_{2(1-x)}Se_{2x}$ 合金的合成及 $MoS_{2(1-x)}Se_{2x}$(x=0.25)场效应晶体管的光电特性[J]. 光学学报, 2022, 42(16): 1616001.
Zhang P R, Liu H, Hu J X, et al. Synthesis of monolayer $MoS_{2(1-x)})Se_{2x}$ alloy and photoelectric properties of $MoS_{2(1-x)})Se_{2x}$ (x=0.25) field-effect transistor[J]. Acta Optica Sinica, 2022, 42(16): 1616001.
[16] 李江霖, 孙科学. 基于纳米金属修饰的石墨烯光电探测器光吸收特性研究[J]. 激光与光电子学进展, 2022, 59(21): 2124003.
Li J L, Sun K X. Light absorption characteristics of a graphene photodetector based on nano-metal modification[J]. Laser & Optoelectronics Progress, 2022, 59(21): 2124003.
[17] Liu X Y, Wu S X, Cao X X, et al. Plasmon resonance-enhanced graphene nanofilm-based dual-band infrared silicon photodetector[J]. Photonics Research, 2023, 11(10): 1657.
[18] Zhang H. Ultrathin two-dimensional nanomaterials[J]. ACS Nano, 2015, 9(10): 9451-9469.
[19] Wang F, Wang Z X, Shifa T A, et al. Two-dimensional non-layered materials: synthesis, properties and applications[J]. Advanced Functional Materials, 2017, 27(19): 1603254.
[20] Manzeli S, Ovchinnikov D, Pasquier D, et al. 2D transition metal dichalcogenides[J]. Nature Reviews Materials, 2017, 2(8): 17033.
[21] Ramasubramaniam A. Large excitonic effects in monolayers of molybdenum and tungsten dichalcogenides[J]. Physical Review B, 2012, 86(11): 115409.
[22] Ghosh S, Su R, Zhao J X, et al. Microcavity exciton polaritons at room temperature[J]. Photonics Insights, 2022, 1(1): R04.
[23] Barnes W L, Dereux A, Ebbesen T W. Surface plasmon subwavelength optics[J]. Nature, 2003, 424: 824-830.
[24] Gramotnev D K, Bozhevolnyi S I. Plasmonics beyond the diffraction limit[J]. Nature Photonics, 2010, 4: 83-91.
[25] Kasprzak J, Richard M, Kundermann S, et al. Bose–Einstein condensation of exciton polaritons[J]. Nature, 2006, 443: 409-414.
[26] Lerario G, Fieramosca A, Barachati F, et al. Room-temperature superfluidity in a polariton condensate[J]. Nature Physics, 2017, 13: 837-841.
[27] Sillanpää M A, Park J I, Simmonds R W. Coherent quantum state storage and transfer between two phase qubits via a resonant cavity[J]. Nature, 2007, 449: 438-442.
[28] Zasedatelev A V, Baranikov A V, Sannikov D, et al. Single-photon nonlinearity at room temperature[J]. Nature, 2021, 597: 493-497.
[29] Wang S J, Li S L, Chervy T, et al. Coherent coupling of WS_2 monolayers with metallic photonic nanostructures at room temperature[J]. Nano Letters, 2016, 16(7): 4368-4374.
[30] Li B W, Zu S, Zhang Z P, et al. Large Rabi splitting obtained in Ag-WS_2 strong-coupling heterostructure with optical microcavity at room temperature[J]. Opto-Electronic Advances, 2019, 2(5): 190008.
[31] Sang Y G, Wang C Y, Raja S S, et al. Tuning of two-dimensional plasmon-exciton coupling in full parameter space: a polaritonic non-Hermitian system[J]. Nano Letters, 2021, 21(6): 2596-2602.
[32] Zheng D, Zhang S P, Deng Q, et al. Manipulating coherent plasmon-exciton interaction in a single silver nanorod on monolayer WSe_2[J]. Nano Letters, 2017, 17(6): 3809-3814.
[33] Han X B, Wang K, Xing X Y, et al. Rabi splitting in a plasmonic nanocavity coupled to a WS_2 monolayer at room temperature[J]. ACS Photonics, 2018, 5(10): 3970-3976.
[34] Geisler M, Cui X M, Wang J F, et al. Single-crystalline gold nanodisks on WS_2 mono- and multilayers for strong coupling at room temperature[J]. ACS Photonics, 2019, 6(4): 994-1001.
[35] Yang L L, Xie X, Yang J N, et al. Strong light-matter interactions between gap plasmons and two-dimensional excitons under ambient conditions in a deterministic way[J]. Nano Letters, 2022, 22(6): 2177-2186.
[36] Liu L, Tobing L Y M, Yu X C, et al. Strong plasmon-exciton interactions on nanoantenna array-monolayer WS_2 hybrid system[J]. Advanced Optical Materials, 2020, 8(5): 1901002.
[37] Sun J W, Li Y, Hu H T, et al. Strong plasmon-exciton coupling in transition metal dichalcogenides and plasmonic nanostructures[J]. Nanoscale, 2021, 13(8): 4408-4419.
[38] Wen J X, Wang H, Wang W L, et al. Room-temperature strong light-matter interaction with active control in single plasmonic nanorod coupled with two-dimensional atomic crystals [J]. Nano Letters, 2017, 17(8): 4689-4697.
[39] Cuadra J, Baranov D G, Wersäll M, et al. Observation of tunable charged exciton polaritons in hybrid monolayer WS_2-plasmonic nanoantenna system[J]. Nano Letters, 2018, 18(3): 1777-1785.
[40] Palik E D, Lowrie W. Handbook of optical constants of solids [M]. San Diego: Academic Press, 1998
[41] Weber M J. Handbook of optical materials[M]. Boca Raton: CRC Press, 2003.
[42] Xie H, Kong F M, Li K. The electric field enhancement and resonance in optical antenna composed of AU nanoparicles[J]. Journal of Electromagnetic Waves and Applications, 2009, 23(4): 534-547.
[43] Ansari N, Ghorbani F. Light absorption optimization in two-dimensional transition metal dichalcogenide van der Waals heterostructures[J]. Journal of the Optical Society of America B Optical Physics, 2018, 35(5): 1179-1185.
[44] Fan S H, Suh W, Joannopoulos J D. Temporal coupled-mode theory for the Fano resonance in optical resonators[J]. Journal of the Optical Society of America A, 2003, 20(3): 569-572.
[45] Lu H, Liu X M. Optical bistability in subwavelength compound metallic grating[J]. Optics Express, 2013, 21(11): 13794-13799.
[46] Taflove A, Hagness S C. Computational electrodynamics: the finite-difference time-domain method[M]. 3rd ed. Boston: Artech House, 2005.
[47] Lu H, Shi S H, Li D K, et al. Strong self-enhancement of optical nonlinearity in a topological insulator with generation of Tamm state[J]. Laser & Photonics Reviews, 2023, 17(10): 2300269.
[48] Yeshchenko O A, Bondarchuk I S, Gurin V S, et al. Temperature dependence of the surface plasmon resonance in gold nanoparticles[J]. Surface Science, 2013, 608: 275-281.
[49] Xu M, Yang J Y, Zhang S Y, et al. Role of electron-phonon coupling in finite-temperature dielectric functions of Au, Ag, and Cu[J]. Physical Review B, 2017, 96(11): 115154.
[50] Jauffred L, Samadi A, Klingberg H, et al. Plasmonic heating of nanostructures[J]. Chemical Reviews, 2019, 119(13): 8087-8130.
[51] Hutter E, Fendler J H. Exploitation of localized surface plasmon resonance[J]. Advanced Materials, 2004, 16(19): 1685-1706.

[52] Wei H, Yan X H, Niu Y J, et al. Plasmon-exciton interactions: spontaneous emission and strong coupling[J]. Advanced Functional Materials, 2021, 31(51): 2100889.
[53] Chen W J, Li M, Zhang W H, et al. Dual-resonance sensing for environmental refractive index based on quasi-BIC states in all-dielectric metasurface[J]. Nanophotonics, 2023, 12(6): 1147-1157.

Strong Coupling Between Surface Plasmons in Metallic Grating and Excitons in Tungsten Disulfide

Su Yingwen[1], Lu Hua[1*], Shi Shouhao[1], Li Dikun[1], Wang Xiangxian[2], Zhao Jianlin[1**]

[1]*Key Laboratory of Light Field Manipulation and Information Acquisition, Ministry of Industry and Information Technology, School of Physical Science and Technology, Northwestern Polytechnical University, Shaanxi Key Laboratory of Optical Information Technology, Xi'an* 710129, *Shaanxi, China*;

[2]*School of Science, Lanzhou University of Technology, Lanzhou* 730050, *Gansu, China*

Abstract

Objective In recent years, strong coupling between surface plasmons and excitons has become a research hotspot in light-matter interactions. As an important two-dimensional material, transition metal dichalcogenides (TMDs) have caught extensive attention due to their unique optoelectrical properties. TMD monolayers are direct band gap semiconductors and their excitons have large transition dipole moments and binding energy, which is beneficial to realize the strong coupling between photons and excitons at room temperature. Surface plasmons in metallic nanostructures feature near-field enhancement and small mode volume, providing an effective platform for realizing its strong coupling with excitons. Recently, the strong coupling has been achieved between surface plasmons and TMD excitons in plasmonic systems such as metallic nanoarray, nanoparticles, and nanocavities. One-dimensional (1D) metallic grating is a typical plasmonic structure, in which the coupling effect between surface plasmons and TMD excitons has been rarely studied till now. Thus, we investigate the plasmon-exciton strong coupling behavior in the 1D metallic grating integrated with monolayer tungsten disulfide (WS_2).

Method We build a simulation model by adopting the finite-difference time-domain (FDTD) method and numerically investigate the coupling effect between surface plasmons in the gold grating and excitons in monolayer WS_2. The dielectric constants of gold and monolayer WS_2 are described by the Drude model and high-order Lorentz model respectively. The spectral response and electric field distribution of the gold grating structure and gold grating/monolayer WS_2 hybrid structure are calculated. We study the dependence of reflection spectra on the structural parameters (grating pitch p, width l, and height h) in the gold grating and gold grating/monolayer WS_2 hybrid structures. Based on the temporal coupled-mode theory, we build a model of optical coupling between surface plasmons in the gold grating and excitons in monolayer WS_2 and thus derive the theoretical formula of the reflection spectrum from the hybrid structure. The temporal coupled-mode theory is employed to fit the reflection spectra of the hybrid structures. Thus, we obtain the fitting parameters containing plasmonic and exciton decay rates and coupling strength in the hybrid structures with different grating heights. Then, the coupled oscillator model is utilized to calculate the splitting energy of the reflection spectra from the gold grating/monolayer WS_2 hybrid structures. Finally, the dependence of the reflection spectrum on the environmental refractive index is studied by FDTD simulation.

Results and Discussions The results show that the reflection spectrum of the gold grating with the pitch $p = 400$ nm, width $l = 300$ nm, and height $h = 95$ nm possesses an obvious dip at the wavelength of 620 nm due to the generation of surface plasmons. When the monolayer WS_2 is integrated with the gold grating, the plasmonic reflection spectrum will be split. There is an obvious reflection peak at 620 nm wavelength in the original reflection dip with two reflection dips around the peak [Fig. 1(b)]. The electric field of the gold grating is mainly localized at the vertex of the gold grating. With a monolayer WS_2, the electric field intensity is weakened [Figs. 1(c) and 1(d)]. With the increasing pitch, width, and height, the reflection dip of the gold grating has a red-shifted [Figs. 2(a), 3(a), and 4(a)]. The reflection spectra of the hybrid structure are fitted by the temporal coupled-mode theory, and they are in good agreement with the simulated spectra [Figs. 2(b), 3(b), and 4(b)]. We find that the fitted decay rate and coupling strength are not sensitive to the height of the gold grating, and the plasmonic resonance frequency decreases with increasing h (Fig. 5). The analyzed results yielded by

the coupled oscillator model show that the coupling between the surface plasmons and the excitons in the hybrid structure satisfies the criterion of strong coupling with the Rabi splitting of 54.6 meV (Fig. 6). The relationship between the coupling spectrum and environmental refractive index is studied in the hybrid structure. The wavelength difference between the two reflection dips is found to be approximately linear with the refractive index, which provides a possible way for optical sensing (Fig. 7).

Conclusions The coupling characteristics of surface plasmons in the gold grating and excitons in monolayer WS_2 are studied. The spectral response and electric field distribution of the 1D gold grating/monolayer WS_2 hybrid structure are simulated by the FDTD simulation. The results show that the coupling between surface plasmons in the gold grating and excitons in monolayer WS_2 can generate spectral splitting. The reflection spectra of the hybrid structure with different structural parameters are fitted by adopting the temporal coupled-mode theory. The fitting results are in good agreement with the numerical simulation. The theoretical analysis shows that the coupling between surface plasmons in the gold grating and excitons in the monolayer WS_2 satisfies the strong coupling criterion. The Rabi splitting of coupling spectra from the hybrid structure is 54.6 meV, which is consistent with the temporal coupled-mode theoretical result. The simulation results show that the wavelength difference between the spectral dips of strong coupling presents nearly linear relations with the environmental refractive index, which will offer a new way for optical sensing. Additionally, this work will provide a new method for plasmon-exciton strong coupling in metallic grating integrated with TMDs and its applications in optical devices.

Key words surface plasmons; one-dimensional gold grating; tungsten disulfide; excitons; strong coupling